Serbian Tribology Society

SERBIATRIB '25

19th International Conference on Tribology

Faculty of Engineering University of Kragujevac

Kragujevac, Serbia, 14 – 16 May 2025

Research paper DOI:10.24874/ST.25.129

EFFECT OF W, Ni, AND Co DOPING ON THE MICROSTRUCTURE, CORROSION RESISTANCE, AND WEAR BEHAVIOR OF IRON-BASED ALLOYS PROCESSED BY SOLID-STATE SINTERING

Mebarki LAHCENE[1], Hammoudi ABDERRAZAK[2,3], Guendouz HASSAN[1], Ivana ATANASOVSKA[4,*]

[1]Center of research in mechanics, Constantine, Algeria

[2]UR-MPE, M'hamed Bougara University, Boumerdes, Algeria

[3]Applied Precision Mechanics Laboratory, Institute of Optics and Precision Mechanics, Setif-1-University, Algeria

[4]Mathematical Institute of the Serbian Academy of Sciences and Arts, Belgrade, Serbia,

*Corresponding author:iatanasovska@mi.sanu.ac.rs, iviatanasov@yahoo.com

Abstract: *This study synthesizes iron-based alloys with compositions of 85Fe–3C–10W–5Ni, 85Fe–3C–10W–5Co, and 80Fe–3C–10W–5Ni–5Co via sintering at 1400°C. The primary objective is to evaluate the influence of nickel (Ni), cobalt (Co), and tungsten (W) on the microstructure, corrosion, and wear resistance of the produced alloys. Among the tested compositions, the alloy containing both W and Ni exhibited the most favorable overall performance, particularly in terms of corrosion and wear resistance. The measured friction level is 0.42, and the wear rate is found to be 2.8 × 10^{-5} $mm^3 \cdot N^{-1} \cdot m^{-1}$, showing that it performs very well in reducing friction and wear. X-ray photoelectron spectroscopy (XPS) analysis showed that thick and strong protective layers formed on the alloy surfaces, which greatly improved corrosion resistance by acting as shields in harsh conditions. We identify abrasive wear, fatigue, and oxidative wear as the predominant wear mechanisms. In general, adding Ni and W greatly enhances the strength and durability of iron-based alloys, making them strong options for tough uses where resistance to wear and rust is crucial, like in mechanical and aerospace engineering.*

Keywords: *iron-based alloy, corrosion, wear, applied load, sliding velocity*

1. INTRODUCTION

The powder metallurgy (P/M) production method offers numerous advantages over conventional manufacturing techniques, such as casting. One of its key benefits is the ability to produce components that are near-net shape, significantly reducing the need for secondary finishing operations like machining. Additionally, P/M processes generally consume less energy, making them both cost-effective and environmentally sustainable. P/M also enables the production of parts with excellent dimensional accuracy, superior surface quality, and high repeatability [1], [2], [3]. These qualities make it an ideal choice for manufacturing precision components. As a result, powder metallurgy is widely employed in the production of jet engine parts, self-lubricating bearings, gears, armor-piercing projectiles, nuclear reactor components, and various

automotive applications [4]. The technical application of bulk iron-based alloys is greatly limited by their intrinsic brittleness and low ductility at room temperature [5]. Austenitic stainless steels are known for their excellent mechanical strength, ductility, and corrosion resistance, outperforming most non-ferrous metals [5]. However, their wear resistance remains relatively low. In recent years, research has focused on enhancing the tribological properties of sintered steels by incorporating various reinforcement particles, without compromising their mechanical strength or corrosion resistance [6, 7]. A wide range of reinforcement materials have been used in steel matrix composites, such as W TiC, Al_2O_3, NbC, and SiC [7, 8, 10, 11].

For example, [11] investigated the effects of TiB_2 particles on the tribological performance of Fe3CWNi stainless steel, reporting that increased TiB_2 content led to continuous improvements in wear resistance. Similarly, [9] fabricated 304 stainless steel matrix composites reinforced with TiB_2 via hot pressing and observed significant enhancements in both mechanical and tribological performance. In another study, [12] examined the fatigue and fracture behavior of Fe3CWNi stainless steel composites reinforced with 10% W, revealing that while W reduced the composite's density and improved its mechanical strength, it also decreased its fracture toughness. [15] studied the high-temperature oxidation behavior of Ni-reinforced composites and found that fine Co particles improved oxidation resistance. Additionally, [7] produced stainless steel matrix composites with up to 5 vol% Ni using arc melting under an argon atmosphere. Although the addition of Ni significantly increased the hardness of AISI 440 stainless steel, it also led to a reduction in chromium content in the matrix, potentially compromising corrosion resistance. [13] Investigated ferritic stainless steel composites containing Co and reported improvements in yield strength, tensile strength, and creep resistance.

Moreover, [14] studied the structure and properties of Fe3CWNi matrix composites reinforced with C and emery powder, concluding that the incorporation of 5Co% emery powder via microwave sintering yielded the most favorable mechanical and physical properties among the composites tested. The choice of manufacturing method also plays a crucial role in the final properties of steel matrix composites. Arc melting techniques can produce composites with high density and good mechanical properties, but the high temperatures involved (>1400 °C) may trigger undesirable reactions between the matrix and the reinforcements, such as chromium depletion in stainless steels. Modern powder metallurgy (PM) techniques—including spark plasma sintering (SPS), high-pressure high-temperature (HP-HT) processing, and hot isostatic pressing (HIP)—can also yield high-density, high-stiffness steel matrix composites [9, 16, 17]. However, their high costs and low productivity limit their widespread use. In contrast, hot pressing is a cost-effective and widely used industrial method that enables near-net shape fabrication, reducing the need for post-processing such as machining [9, 18]. Although extensive studies have been conducted on stainless steel matrix composites reinforced with various particles, there remains a need to better understand the effects of less commonly used reinforcement elements such as tungsten (W), nickel (Ni), and cobalt (Co). In particular, the influence of carbon (C) additions on surface-related properties, such as corrosion and wear resistance, has not been thoroughly investigated to date.

This study investigates iron-based alloys synthesized via sintering at 1400 °C to assess the effects of Ni, Co, and W on their microstructure, corrosion, and wear resistance. The alloy containing both W and Ni demonstrated the best overall performance, especially in resisting corrosion and wear. It showed a low coefficient of friction (0.42) and a wear rate of 2.8×10^{-5} $mm^3 \cdot N^{-1} \cdot m^{-1}$. XPS analysis revealed the formation of dense protective films that significantly enhanced corrosion resistance. The main wear mechanisms were abrasive, fatigue, and oxidative wear, and the improved alloys are well-suited for demanding applications in mechanical and aerospace fields.

2. EXPERIMENTAL PROCEDURE

Samples of Fe3CWNi, Fe3CWCo, and Fe3CWNiCo alloys were made by mixing high-purity powders (Fe3C, W, Ni, Co) for 10 hours in a stainless-steel container. The samples were pressed into cylindrical shapes and subjected to corrosion and wear tests in NaCl and HCl solutions, simulating marine and acidic environments. To simulate tribocorrosion conditions, we applied loads of 5 N and 10 N at a sliding velocity of 5 m/s. Wear was measured using profilometry, and corrosive effects were evaluated through mass loss and microscopic observation. This procedure allows for the evaluation of the tribological performance of the materials, including the friction coefficient and wear rate.

3. RESULTS AND DISCUSSION

3.1. Green and Sintered Densities

Various types of alloy powders were compacted into parallelepiped-shaped samples. This geometry facilitates accurate dimension measurements, allowing precise volume calculations. We determined the density both before and after sintering (Figure 1), i.e., green and sintered states, using the sample weights. The sintered steel samples were also analyzed using helium pycnometry to measure their density. The measured values closely matched the calculated ones (as shown in Table 1). The sintered density was found to be slightly higher than the green density. This difference is due to the shrinkage that happens when sintering, the release of trapped lubricants before sintering, and the way particles come together, which lowers the number of tiny holes and raises the overall density.

3.2. Microhardness

The microhardness of Fe_3CW-based alloys increases with the Ni/Co ratio, ranging from 750 HV to 885 HV (Figure 2). This improvement is linked to the transformation of carbon into a solid solution during sintering, a process influenced by the applied temperature. Alloys with higher Ni/Co ratios generally undergo longer sintering durations, resulting in finer grain structures, which contribute to enhanced hardness. Additionally, reducing the applied load during micro-hardness testing further increases hardness values due to more localized plastic deformation.

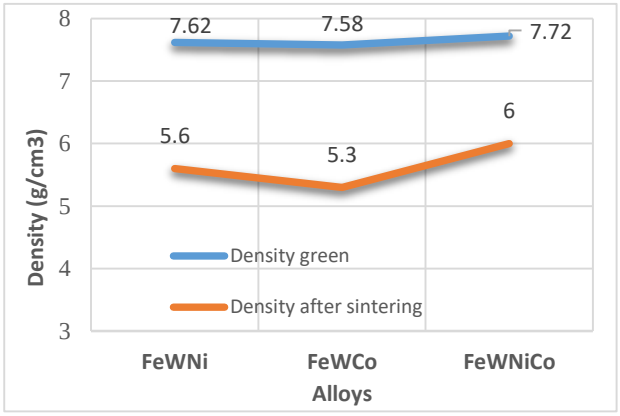

Figure 1. Density before and after sintering

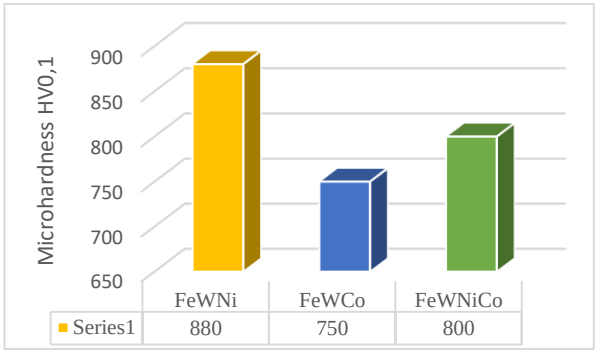

Figure 2. Microhardness

3.3. X-ray Diffraction (XRD)

XRD analysis (Figure 3) revealed that the sintered alloys maintained a phase composition similar to that of the starting powders, primarily dominated by FeW phases. However, slight peak shifts in the Ni/Co regions toward lower angles were observed, indicating structural changes within the matrix. The presence of γ-austenite and δ-ferrite phases was confirmed, with moderate concentrations of δ-ferrite particularly observed in the FeWNiCo alloy. These findings highlight the critical importance of sintering conditions in controlling phase evolution and, therefore, optimizing the mechanical and physical properties of the final alloys.

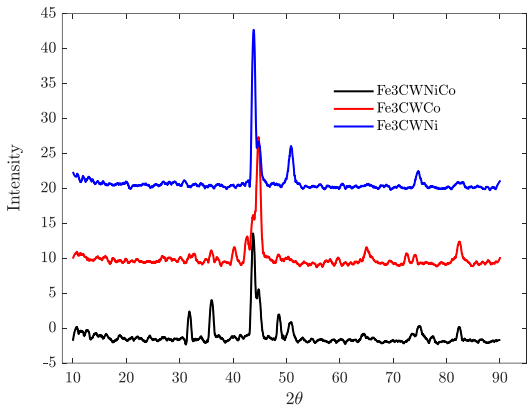

Figure 3. X-ray diffraction (XRD)

3.4. Corrosion Testing

NaCl Solution. This technique allows monitoring of the evolution of the open-circuit potential (OCP) as a function of immersion time in a 3.5% NaCl solution, which simulates a seawater environment. According to Figure 4, the Fe_3CWNi sample shifts toward less noble potentials upon initial immersion—starting at -349 mV, then stabilizing at around -374 mV after one hour. This behavior suggests low corrosion resistance in the presence of chloride ions (Cl^-), likely due to dissolution of carbon within the austenitic (γ) matrix. In contrast, the $Fe_3CWNiCo$ sample begins at -335 mV, stabilizing after around 1000 seconds at -336 mV. When compared with the annealed state of the Fe_3CWNi alloy, the $Fe_3CWNiCo$ sample exhibits a more noble corrosion potential, indicating improved corrosion resistance. This enhancement is likely due to solution treatment, which promotes the formation of protective chromium oxide films.

According to Figure 4, the Fe_3CWNi sample does not show a clear passivation plateau, evident from the increase in current with increasing potential, indicating that no protective film is formed. In contrast, both $Fe_3CWNiCo$ samples exhibit distinct passivation plateaus, confirming the formation of protective oxide layers on their surfaces. Based on the summary table of electrochemical parameters, we can conclude that $Fe_3CWNiCo$ has the most noble corrosion potential among the tested alloys, further confirming its superior corrosion resistance in NaCl environments.

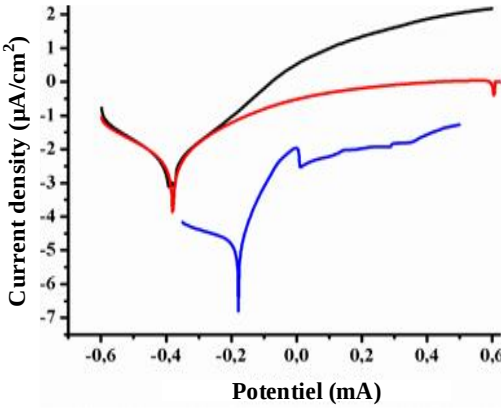

Figure 4. Tafel polarization curves of the sintered Fe_3CWNi, Fe_3CWCo, and $Fe_3CWNiCo$ alloys in a 3.5% NaCl

Table 1: Tafel Polarization Test Results in 3.5% NaCl Solution

Alloys	Eocp (Mv)	Ecor (Mv)	Ecor (Ua)	Vcor (mm/an)
Fe3CWNi	-374	-383.713	3.717	0.021829
Fe3CWCo	-369	-381.252	2.645	0.015533
Fe3CWNiCo	-0.88	-178.092	0.015	88.0923e-6

HCl Solution. The Tafel polarization curves in hydrochloric acid (HCl) solution—also used to simulate an aggressive marine environment—are shown in Figure 5. According to the figure, both Fe_3CWNi and Fe_3CWCo exhibit a shift of corrosion potential toward more positive values, indicating an improved corrosion behavior in HCl medium compared to NaCl. Among the tested samples, Fe_3CWCo shows the lowest corrosion rate at 1.82×10^{-6} mm/year, outperforming both $Fe_3CWNiCo$ and Fe_3CWNi, which have corrosion rates of 46.387×10^{-6} mm/year and 28.992×10^{-6} mm/year, respectively. This difference is attributed to its microstructure, consisting of austenite + eutectic + carbide phases at grain boundaries. The presence of tungsten carbides (W_xC_y) at the grain boundaries may locally reduce the tungsten concentration, increasing the alloy's susceptibility to intergranular corrosion. When comparing the performance of Fe_3CWNi and Fe_3CWCo alloys in different media (NaCl and HCl), we observe that chloride ions (Cl^-) in the

NaCl environment cause greater corrosion. Therefore, these materials exhibit better corrosion resistance in acidic HCl media than in saline environments.

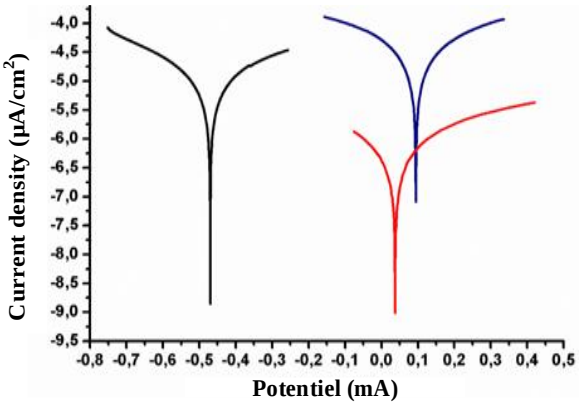

Figure 5. Tafel polarization curves of Fe_3CWNi, Fe_3CWCo, and $Fe_3CWNiCo$ alloys in hydrochloric acid (HCl)

3.5. Tribological Behavior

Tribological tests were carried out using a ball-on-disc tribometer, in which the tested sample slides against a stationary 100C6 steel ball under an applied normal load. Across all samples, there was no observable running-in period—wear began immediately, following specific wear mechanisms. For the Fe_3CWNi sample, the friction coefficient initially starts at $\mu = 0.46$, and reaches a steady-state value of $\mu = 0.53$ after approximately 250 seconds under both 5 N and 10 N loads (Figure 6).

The tribological behavior of the tested sintered steels primarily depends on factors such as manufacturing process, chemical composition, porosity, and prior heat treatments [18]. Preliminary tests over a 20-meter sliding distance with a 5 N load were performed to optimize parameters for this study. The friction coefficient curves are presented in Figure 6. During the initial stage (0–10 m), considered the running-in phase, there is a rapid increase in the friction coefficient from 0.3 to 0.53–0.65, due to asperity flattening and plastic deformation caused by the penetration of the steel ball into the metallic matrix. Beyond 10 m, the surface hardens, resulting in the stabilization of the friction coefficient.

In the cases of Fe_3CWNi and Fe_3CWCo, irregularities in the friction curves confirm surface processes such as cyclical plastic strain (ε_p) – strain hardening – brittle fracture. The effect of solid-state sintering on the surface is clearly observed in the low initial friction values (0–5 m), followed by a monotonic increase in the coefficient of friction without visible stabilization for the samples sintered for 2 hours. For the $Fe_3CWNiCo$ alloy containing 1.2% C, the friction curve shows significant fluctuations starting at 12 m of sliding, likely due to brittle degradation of the running-in layer and the formation of a third body composed of oxide particles detached from the surface. Conversely, a lower-carbon $Fe_3CWNiCo$ sample exhibits a smoother curve with no significant disruptions, indicating abrasive wear without particle detachment. The friction coefficient stabilizes after 15 m of sliding, with no noticeable surface damage. In the case of Fe_3CWNi and Fe_3CWCo alloys subjected to prolonged sintering (2 hours), the behavior changes: the initial friction coefficient is very low ($Cf \approx 0.1$), but increases significantly after 15 m to reach values around 0.6.

Evolution of the Friction Coefficient. Tribological tests were performed over a sliding distance of 250 meters, at a sliding speed of 5 cm/s under a normal load of 5 N, corresponding to a test duration of approximately 45 minutes for all samples. The evolution of the friction coefficient (μ) provides valuable insights into the wear process, particularly regarding energy dissipation, third-body formation, and the severity of wear. Two distinct frictional behaviors were observed across the alloy series. For the Fe_3CWNi, Fe_3CWCo, and $Fe_3CWNiCo$ alloys, the friction coefficient profiles exhibit erratic fluctuations over varying periods. During the initial surface accommodation phase, μ increases from 0.18 to 0.6 for Fe_3CWNi and Fe_3CWCo within the first 25 meters, and from 0.17 to 0.4 for $Fe_3CWNiCo$ within the first 20 meters. After this initial adaptation, a sharp fluctuation in μ is observed. In particular, the $Fe_3CWNiCo$ alloy shows a drop followed by a rapid increase in μ, reaching 0.85, which then

stabilizes around 75 meters. It may slightly decrease thereafter, stabilizing around 0.75.

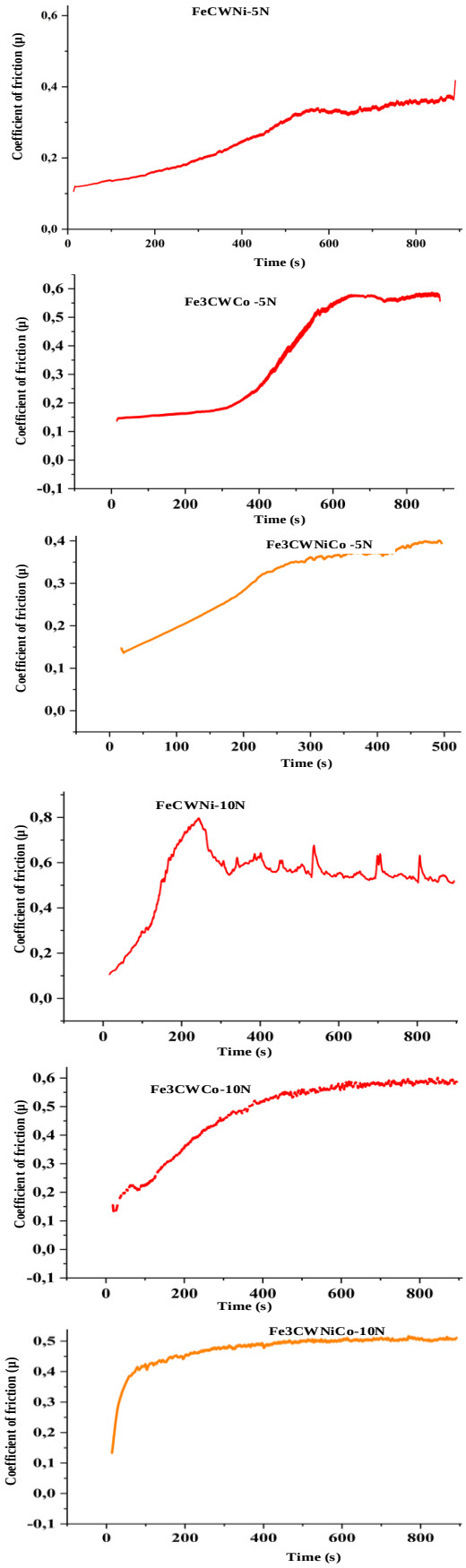

Figure 6. Evolution of the friction coefficient (μ) of alloys

Meanwhile, the μ of $Fe_3CWNiCo$ (with slightly different carbon content) continues to increase until about 0.8, before stabilizing near 0.76 from 210 meters onward. In contrast, Fe_3CWNi displays continuous fluctuations (increase/decrease) throughout the test, with an average friction coefficient of approximately 0.5. However, friction coefficient profiles for the refined Fe_3CWNi, Fe_3CWCo, and $Fe_3CWNiCo$ alloys appear more stable than their counterparts. For instance, $Fe_3CWNiCo$ exhibits a very long running-in period lasting up to 120 meters, after which the coefficient stabilizes around 0.53. On the other hand, Fe_3CWNi shows a rapid increase in μ from 0.15 to 0.7 during the first 25 meters, before gradually stabilizing at 0.75 by the end of the test. Similarly, for $Fe_3CWNiCo$, μ increases from 0.16 to 0.8 over the first 40 meters, eventually stabilizing around 0.8 toward the end of the test.

Wear Mechanism. Microscopic observations of the wear tracks on the test pins confirm the initial analyses derived from the friction curves. As shown in Figure 7, the wear tracks of the softer alloys, where the density of soft and ductile phases is high (Fe_3CWNi, Fe_3CWCo, and $Fe_3CWNiCo$), are characterized by significant material removal (severe wear), manifested by chains of cavities and cracks. On the other hand, the wear tracks of the harder alloys (Fe_3CWNi, Fe_3CWCo, and $Fe_3CWNiCo$) are marked by the presence of a third body trapped in small cavities and on the surface, indicating mild wear. The overall wear behavior is influenced by the progression of wear, which determines the general appearance of the wear track. When the sliding surfaces of the alloys come into contact, strong adhesion occurs at the asperities. This leads to the formation of microsoldering or surface junctions, resulting in adhesive contact. The relative sliding motion then causes these junctions to break at the least hard constituent, leading to material transfer from one surface to the other.

Additionally, wear debris can form, hardened by cold working or oxidation.

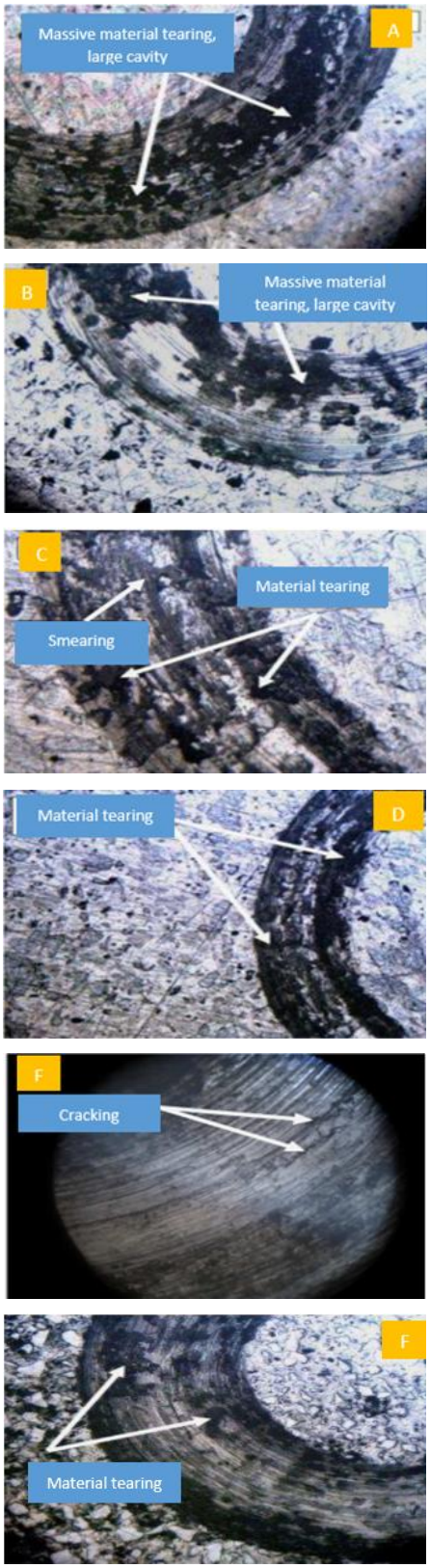

Figure 7: The micrographs of wear tracks for the developed alloys

Sheared wear fragments are transferred to the harder surface, and the softer metal then slides on itself. In some cases, this results in a protective oxide layer forming on the surfaces. The fluctuations seen in the friction coefficient profiles for the Fe_3CWNi, Fe_3CWCo, and $Fe_3CWNiCo$ alloys correspond to seizing stimulated by the presence of soft phases under sufficiently high loads. The spontaneous increase and decrease in the friction coefficient at certain times correspond to the formation of a large number of local junctions during the sliding process. When these junctions cannot be sheared, rupture occurs, facilitated by the increase in tangential force, causing a spontaneous rise in the friction coefficient. However, the rupture of these junctions leads to a drop in the friction coefficient. In some cases, the rupture of these junctions is accompanied by massive material removal in the form of oxidized and cold-worked particles, which may result in abrasive wear.

Evolution of Wear Rate. Tribological tests were conducted to measure the wear rates of the studied alloys over a sliding distance of 250 m, a load of 5 N, and a sliding speed of 10 cm/s. These parameters allowed the wear of the Fe3CWNi, Fe3CWCo, and Fe3CWNiCo alloys to be quantified during the friction process. The results revealed (Table 2) significant differences in the evolution of the wear rate based on the chemical compositions and treatments of the samples. Wear rates were calculated based on the sliding distance and compared among the different alloys. These wear rates mainly depend on the state of the surfaces after the tests, the friction conditions, and the hardness of the materials. Harder alloys exhibited lower wear rates, while softer alloys, such as Fe3CWNi, showed higher wear rates.

Table 2. Wear Rates of Alloys for a Load of 5 N and a Sliding Speed of 10 cm/s

Alloys	Wear Rates $*10^{-5}$ (mm^3/N/m) of (5N)	Wear Rates $*10^{-5}$ (mm^3/N/m) of (10N)
Fe3CWNi	12.07	7.295
Fe3CWCo	2.997	2.415
Fe3CWNiCo	9.122	36.74

The histogram below (Figure 8) highlights the correlation between the wear rate and the

Vickers microhardness. According to this histogram, it is observed that Archard's relation (1) is almost verified; the higher the hardness, the lower the wear rate, except for the Fe3CWNiCo alloy when compared to the Fe3CWNi alloy [17]:

$$V = K \times \frac{P \times L}{H}. \quad (1)$$

where V is the wear volume, k is the wear factor, P is the applied load, L is the distance traveled, and H is the hardness of the soft material.

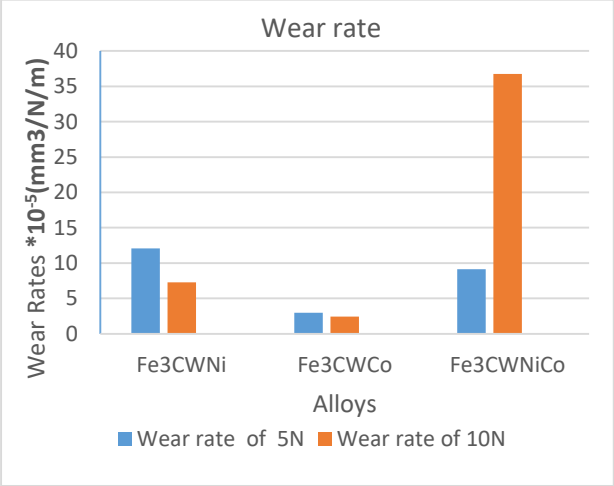

Figure 8. Evolution of the wear rates of alloys

Referring to the previous figure (Figure 8), mechanical buttering was observed, and a significant amount of soft and viscoelastic particles (primarily composed of nickel phases) adhered to the surface, thus filling the pores and the surfaces between the peaks. This phenomenon helps protect the wear surface and facilitates friction. This observation was not noted in the Fe3CWNi alloy.

4. CONCLUSIONS

Iron-based amorphous alloys with varying compositions of 85Fe3CWNi, Fe3CWCo, and Fe3CWNiCo were fabricated using solid-phase sintering at 1400°C. This study examines the effects of doping with Ni, W, and Al on the thermal stability and their influence on the wear and corrosion properties of iron-based alloys. The main conclusions are summarized as follows:

- Microstructural and compositional analyses showed that the iron-based alloys exhibited high mechanical properties, with porosity less than 1%, and good homogenization and distribution of alloying elements. Doping with W, Ni, and Co significantly enhanced the thermal stability of the base iron alloy;
- Potentiostatiques tests and impedance analysis revealed that the W and Ni-doped alloy had the lowest stable current densities and the highest passivation index across various polarization potentials. This superior performance is attributed to the increased fraction of low-valence metal oxides and the formation of the thickest and most protective passive film;
- According to the point defect model, the W and Ni-doped alloy maintains a stable oxidation state during the injection of cations from the barrier layer/solution interface. This stability, attributed to robust W oxides like WO3, facilitates the rapid formation of a thicker passive film while suppressing active metal dissolution, significantly enhancing the corrosion resistance of the coatings;
- Iron-based alloys exhibited high microhardness (750–900 HV0.1), which is superior to that of steels. Dry sliding wear tests revealed superior wear resistance of the iron-based alloys, with a coefficient of friction (COF) ranging from 0.42 to 0.49 and a wear rate of (2.8–11.3) × 10−5 $mm^3 \cdot N^{-1} \cdot m^{-1}$, compared to steel. Notably, the W and Ni-doped alloy demonstrated the best overall wear resistance.

ACKNOWLEDGEMENT

A part of the research has been supported by the Ministry of science, technological development and innovation of Republic of Serbia by Contract number: 451-03-136/2025-03/ 200029.

ORCID iDs

Mebarki LAHCENE
Hammoudi ABDERRAZAK 0000-0001-8911-348X
Guendouz HASSAN
Ivana ATANASOVSKA 0000-0002-3855-4207

REFERENCES

[1] A. Erdogan, A. Günen, M. S. Gök and S. Zeytin, "Microstructure and mechanical properties of borided CoCrFeNiAl0 25Ti0. 5 high entropy alloy produced by powder metallurgy," *Vacuum*, vol. 183, pp. 109820, January 2021, doi: 10.1016/j.vacuum.2020.109820.

[2] A. Erdogan, B. Kursuncu, A. Günen, M. Kalkandelen and M.S. Gok, "A new approach to sintering and boriding of steels "Boro-sintering": Formation, microstructure and wear behaviors," *Surface and Coatings Technology*, vol. 386, pp. 125482, March 2020, doi: 10.1016/j.surfcoat.2020.125482.

[3] F. Martin and J. Ertzberger, "Here and now mobile learning: An experimental study on the use of mobile technology," *Computers & Education*, vol. 68, pp. 76-85, October 2013, doi: 10.1016/j.compedu.2013.04.021.

[4] D. Fernández-Valdés, A. Meneses-Amador, A. López-Liévano and A. Ocampo-Ramírez, "Sliding wear analysis in borided AISI 316L steels," Materials Letters, vol. 285, pp. 129138, February 2021, doi: 10.1016/j.matlet.2020.129138.

[5] S. A. Jose, M. John and P. L. Menezes, "Cermet systems: synthesis, properties, and applications," *Ceramics*, vol. 5, no. 2, pp. 210-236, doi: 10.3390/ceramics5020018.

[6] J. Kübarsepp and J. Kristjan, "Cermets with Fe-alloy binder: A review," *International Journal of Refractory Metals and Hard Materials*, vol. 92Q, pp. 105290, November 2020, doi: 10.1016/j.ijrmhm.2020.105290.

[7] L. Zhang, Y. Gao, Z. Huang, H. Ma, Y. Liu, W. Jie and L. Zhou, "Effect of Ni content on the corrosion behavior of Mo2NiB2–Ni cermet in H2SO4 solution," *Ceramics International*, vol. 49, no. 22, pp. 36289-36298, November 2023, doi: 10.1016/j.ceramint.2023.08.311.

[8] Z. Wang, H. Liu, J. Huang, S. Zhuo, Y. Wu, G. Wang and D. Zeng, "Improving wear and corrosion resistance of HVAF sprayed 316L stainless steel coating by adding TiB2 ceramic particles and CeO2," *Journal of Materials Research and Technology*, vol. 31, pp. 1313-1325, July–August 2024, doi: 10.1016/j.jmrt.2024.06.146.

[9] Z. Jiang, Y. Zheng, W. Ding, Y. Zhao and W. Zhou,"Effect of nano-TiO2 addition on the microstructure and erosion-corrosion behavior of Ti (C, N)-based cermets fabricated by in-situ carbothermal reduction," *International Journal of Refractory Metals and Hard Materials*, vol. 110, pp. 106035, January 2023, doi: 10.1016/j.ijrmhm.2022.106035

[10] J. Tarabay, V. Peres, E. Serris, F. Valdivieso and M. Pijolat, "Zirconia matrix composite dispersed with stainless steel particles: Processing and oxidation behavior," *Journal of the European Ceramic Society*, vol. 33, no. 6, pp. 1101-1110, June 2013, doi: 10.1016/j.jeurceramsoc.2012.11.020

[11] M. Dourandish, A. Simchi, K. Hokamoto and S. Tanaka, "Phase formation during sintering of nanocrystalline zirconia/stainless steel functionally graded composite layers," *Materials letters*, vol. 65, no. 3, pp. 523-526, February 2011, doi: 10.1016/j.matlet.2010.10.077.

[12] X.Pang, I. Zhitomirsky and M.Niewczas, "Cathodic electrolytic deposition of zirconia films," *Surface and Coatings Technology*, vol. 195, no. (2-3), pp. 138-146, May 2005, doi: 10.1016/j.surfcoat.2004.08.216.

[13] I. Gurappa, "Development of appropriate thickness ceramic coatings on 316 L stainless steel for biomedical applications," *Surface and Coatings Technology*, vol. 161, no. 1, pp. 70-78, November 2002, doi: 10.1016/S0257-8972(02)00380-8.

[14] E.Nouri, M.Shahmiri, H. R. Rezaie and F. Talayian, "Investigation of structural evolution and electrochemical behaviour of zirconia thin films on the 316L stainless steel substrate formed via sol–gel process," *Surface and Coatings Technology*, vol. 205, no. (21-22), pp. 5109-5115, August 2011, doi: 10.1016/j.surfcoat.2011.05.024.

[15] Y.Han, W.Zhang, S.Sun, H. Chen and X. Ran, "Microstructure, hardness, and corrosion behavior of TiC-duplex stainless steel composites fabricated by spark plasma sintering," *Journal of Materials Engineering and Performance*, vol. 26, pp. 4056-4063, 2017, doi: 10.1007/s11665-017-2840-2.

[16] O. O.Shichalin, S. B.Yarusova, N. P.Ivanov, E. K.Papynov, A. A.Belov, S. A. Azon and P. S. Gordienko, "Calcium silicate solid-state matrices from boric acid production waste for 60Co removal and immobilization by spark plasma sintering," *Journal of Water Process Engineering*, vol. 59, pp. 105042, March 2024, doi: 10.1016/j.jwpe.2024.105042.

[17] M. Stępień, I. Sulima, P. Hyjek and R. Kowalik,"Evaluation of the corrosion resistance

of spark plasma sintered stainless steel 316L matrix composites with zirconium diboride in sulfuric acid," *Archives of Civil and Mechanical Engineering*, vol. 22, no. 3, pp. 127, 2022, doi: 10.1007/s43452-022-00453-1

[18] A. AlHazaa and N. Haneklaus, "Diffusion bonding and transient liquid phase (TLP) bonding of type 304 and 316 austenitic stainless steel—A review of similar and dissimilar material joints," *Metals*, 10(5), 613, doi: 10.3390/met10050613